applied sciences

MDPI

Article

Revolutionizing Concrete Bridge Assessment: Implementing Nondestructive Scanning for Transformative Evaluation

Wael Zatar *, Felipe Mota Ruiz and Hien Nghiem

Encova Center for Engineering and Safety, Department of Civil Engineering, Marshall University, Huntington, WV 25755, USA; motaruiz@marshall.edu (F.M.R.); nghiem@marshall.edu (H.N.)
* Correspondence: zatar@marshall.edu

Abstract: This study focused on analyzing the impact of ground-penetrating radar (GPR) scan spacing on accurately assessing the reinforcement of concrete bridge girders, providing practical insights. A decommissioned bridge box beam was evaluated to unveil rebars and tendons' depth and spacing. The box beam was decommissioned from the West Virginia Division of Highways inventory. An innovative algorithm was developed to fully automate the analysis of survey grid data across all sides of the beam. Implementing this algorithm into a computer code has paved the way for comprehensive automation of GPR data analyses. Comparing GPR data analyses from various profile line offsets, this study assists in producing optimal protocols for inspecting box beams. Transverse profile line offsets between 4 in. and 24 in. yielded nearly identical results, setting a new standard for precision. Utilizing more than one longitudinal profile line was highly beneficial in accurately assessing prestressed concrete box beams. This research helps redefine bridge evaluation by precisely finding rebar spacing, concrete cover, and other internal characteristics. This study's findings offer invaluable advancements and equip state departments of transportation with the knowledge to accurately assess in-service concrete bridge box beams, empowering them to make informed decisions.

Keywords: reinforced concrete; prestressed concrete; corrosion; deterioration; bridge inspection; bridge assessment; nondestructive testing

check for updates

Citation: Zatar, W.; Ruiz, F.M.; Nghiem, H. Revolutionizing Concrete Bridge Assessment: Implementing Nondestructive Scanning for Transformative Evaluation. *Appl. Sci.* **2024**, *14*, 11590. https://doi.org/10.3390/app142411590

Academic Editors: Raffaele Ciardiello, Donato Perfetto and Alessandro De Luca

Received: 4 November 2024
Revised: 28 November 2024
Accepted: 5 December 2024
Published: 12 December 2024

Copyright: © 2024 by the authors. Licensee MDPI, Basel, Switzerland. This article is an open access article distributed under the terms and conditions of the Creative Commons Attribution (CC BY) license (https://creativecommons.org/licenses/by/4.0/).

1. Introduction

Bridge inspection is essential for ensuring the safety of the public and the stability of the United States economy. It involves evaluating the structural conditions and integrity of bridges through quick, effective, and cost-efficient visual inspections suitable for a variety of structural applications. Additionally, bridge inspection includes the use of simple on-site testing methods to assess the structural integrity of bridges. However, a limitation of bridge inspections is the inability to thoroughly assess internal defects and deteriorations, particularly in reinforced concrete components, which are vital for accurately determining the true conditions of bridge structures. Furthermore, visual bridge inspections are subjective, leading to assessment discrepancies due to significant variations in judgments among different bridge inspectors [1].

Complementing the frequently used visual inspections, nondestructive testing and evaluation (NDT & E) techniques have gained popularity for their efficiency in assessing structures as they provide rapid and reliable assessments of bridge conditions without causing significant damage or interrupting traffic flow. This efficiency underscores their reliability and makes them a valuable tool in bridge inspection and maintenance [2,3].

Among all NDT & E techniques, popular methodologies used to assess reinforced concrete (RC) structures involve acoustic-based and electromagnetic-based methods. Moreover, various assessment techniques are used to evaluate reinforced concrete structures. The acoustic-based assessment methods encompass techniques such as impact echo and

ultrasonic pulse. The electromagnetic-based assessment methods for real-time monitoring [4–6] include ground-penetrating radars, infrared thermography, and radiography. In addition, several NDT methods were widely used to detect the defects in RC structures such as fiber optic sensors [7,8], scanning laser Doppler vibrometer [9], and interfacial waves and transducer [10]. The techniques have demonstrated varying levels of effectiveness in assessing reinforced concrete members, highlighting the need for further research into their application in real-world inspection scenarios. It is, therefore, essential to acknowledge that each of the mentioned assessment techniques has its advantages and limitations depending on the type of reinforced concrete structure being inspected and what the objective of the structural evaluation is [11].

In its early development, the ground-penetrating radar (GPR) system was initially introduced to geophysics for soil exploration. As technology advanced and more sophisticated systems were developed in the early 1990s, the device began to be used in other areas, such as inspecting reinforced concrete structures. The system includes a high-frequency antenna that emits and receives electromagnetic pulses. These pulses travel into the ground or structure and are reflected when they encounter changes in electromagnetic properties due to embedded objects. A computer system then interprets the reflected pulses. The GPR method has been examined to assess bridge decks [12], determine rebar layout and size in concrete structures [13–15], and evaluate the concrete cover and overall thickness of concrete slabs [16,17].

The capabilities of GPR have been extensively studied for various reinforced concrete structure assessments, including evaluating moisture levels [18], mapping deterioration in aging bridge decks [19], monitoring cracks [20], detecting rebar corrosion in concrete slabs [21,22], visualizing embedded defects [23], identifying voids in grouted post-tensioned concrete ducts [24], assessing the impact of concrete mix variations and environmental conditions on defect detection [25], identifying anomalies in corrosion-induced bridge decks [26], visualizing defects in fiber-reinforced polymer-wrapped reinforced concrete slabs [27], and mapping rebar layers within reinforced concrete [28], and advanced techniques have been developed for GPR signal processing [29]. The influence of environmental factors on GPR signals has also been analyzed [30]. Both chloride content in concrete and rebar corrosion were found to reduce GPR reflection amplitudes. Moreover, higher chloride content resulted in greater attenuation of GPR signals. Higher temperatures also resulted in stronger amplitude attenuation, with concrete containing higher chloride levels exhibiting greater sensitivity to temperature variations. In contrast, relative humidity was found to have an insignificant effect on GPR signal reflection amplitudes.

The analysis and interpretation of GPR data are often challenging and labor-intensive, demanding substantial expertise and computational effort to derive meaningful insights. Implementing a fully automated GPR data interpretation system for identifying embedded rebars could effectively address this challenge [31–33].

Zatar et al. [34] proposed a new approach based on a synthetic aperture technique that has proven effective in providing rebar layout information, including rebar spacing, depth, and concrete cover. Zatar et al. [35] presented a revolutionizing methodology using curve fitting principles to simultaneously determine the rebars' horizontal location, depth, concrete cover, and size.

This study aimed to identify the optimal transverse and longitudinal GPR profile line spacing offset. The approach involved calculating the depth and spacing of rebars on each face of the beam by measuring the electromagnetic wave travel time. A series of GPR scans was conducted at various offsets, and the resulting hyperbolas were analyzed. A computer code was developed using Delphi programing language to automatically compute the rebars' location by detecting all hyperbolic reflections from the GPR radargrams and best fitting them with proposed equations. This study has proven to be an efficient and reliable method for estimating rebars' horizontal and vertical locations in concrete structures. This study comprehensively explores GPR's capabilities in assessing reinforced concrete

structures, providing valuable insights into advancements in nondestructive testing and evaluation methods for inspection and maintenance of the bridges.

2. Research Significance

Current studies offer limited insights into the effects of GPR scan spacing on effectively assessing internal deficiencies of structural concrete members, such as voids, delaminated areas, and locations of reinforcement corrosion and section loss. Recent research has limited information on how the GPR technology can effectively be employed to inspect prestressed concrete box beams and determine the rebars' depth, spacing, and size. This research addresses the knowledge gaps of GPR and suggests an accurate assessment of in-service bridges. This study employs a prestressed concrete box beam of a decommissioned bridge from the West Virginia Division of Highways inventory. The research study aims at enhancing the ability of bridge inspectors to assess the condition of bridge box beams more precisely and effectively in the field. The improved evaluation capability will assist state and federal agencies in allocating their financial and human resources more effectively. This study will ensure efficient and more informed transportation infrastructure investment decisions and potentially save significant costs in the long run.

3. GPR System and Data Processing

Ground-penetrating radar is a system that operates by emitting electromagnetic (EM) waves into the subsurface. The computer system then generates an image by analyzing the radar pulses reflected from objects inside the media being analyzed. These waves are transmitted by the transmitting antenna and captured by the receiver when embedded objects reflect them. Civil engineering applications typically have a wave frequency between 20 MHz and 2.5 GHz. Two crucial physical properties influence the propagation of the EM waves in the subsurface: the dielectric constant of the EM waves and the electrical conductivity of the subsurface.

The conductivity of the subsurface plays a pivotal role in the propagation and attenuation of the EM pulses. Low-conductivity materials, such as dry sand, ice, and dry concrete, are the perfect candidates for GPR. They facilitate the EM waves to travel to greater depths with minimal energy loss. On the other hand, high-conductive materials, like saltwater and wet concrete, absorb radar energy before the EM pulses can penetrate deep into the subsurface. This precision makes GPR an ideal method for examining materials like dry concrete, wood, sand, and asphalt, instilling confidence in its capabilities.

Along with the materials' conductivity, the dielectric constant is a critical physical property in the analysis of the GPR data. The dielectric constant determines the speed at which EM pulses travel into the subsurface. Given the velocity of electromagnetic waves, multiplying the two-way travel time from the transmitter to the receiver by the electromagnetic speed provides the object's depth in the material. Electromagnetic waves propagate through air at a speed nearly equal to the speed of light, corresponding to a dielectric constant of 1, while, in water, their velocity is approximately one ninth that of light, with a dielectric constant of 81. For most construction materials, wave velocities range from 3.5 to 7.0 inches per nanosecond, corresponding to dielectric constants between 12 and 3 [36].

The GPR data are collected and stored in a two-dimensional matrix, representing the signal reflection based on depth and the horizontal position of the radar. In the radargram, the signal is visualized as a color spectrum transitioning from dark blue to dark red on the jet-color scale, corresponding to signal amplitudes ranging from minimum negative to maximum positive.

When an electromagnetic wave is emitted into the material, it travels at a constant dielectric speed until it encounters a material with a different dielectric constant, such as rebars, moisture, delamination, and air voids. This difference in material properties is reflected in the receiver and detected by the system. The more exponential the difference between the two materials is, the stronger the reflected waves will be. Rebars in concrete,

for instance, show intense reflections because of the conductivity difference between steel and concrete.

The GPR system (GSSI SIR-4000) (Geophysical Survey Systems, Inc. (GSSI), 40 Simon Street, Nashua, NH 03060-3075, USA) used in this research is a comprehensive setup, comprising a 1.6 GHz antenna with transmitter and receiver spacing (T-R offset) of 2.3 in. The system used in this paper is illustrated in Figure 1. To ensure data accuracy, a "background removal" method was employed to eliminate surface deflection noise (i.e., direct coupling) pulses.

Figure 1. GPR system.

4. Experimental Program

4.1. Laboratory Precast Prestressed Concrete Box Beam

The West Virginia Division of Highways has supplied a precast prestressed concrete box beam from a decommissioned bridge in Cabell County, West Virginia. The concrete box beam measures 32.5 ft in length, 3.0 ft in width, and 17 in. in height, as depicted in Figure 2. The beam's reinforcement includes four #4 longitudinal rebars at the top, stirrups typically spaced at 12 in., two sets of five prestressed tendons at the bottom of the beam, and a prestressed tendon positioned at the beam's centerline. Besides the reinforcement, the concrete beam contains two 10 in. diameter voids. Figures 2 and 3 illustrate the concrete box beam's typical section and plan view.

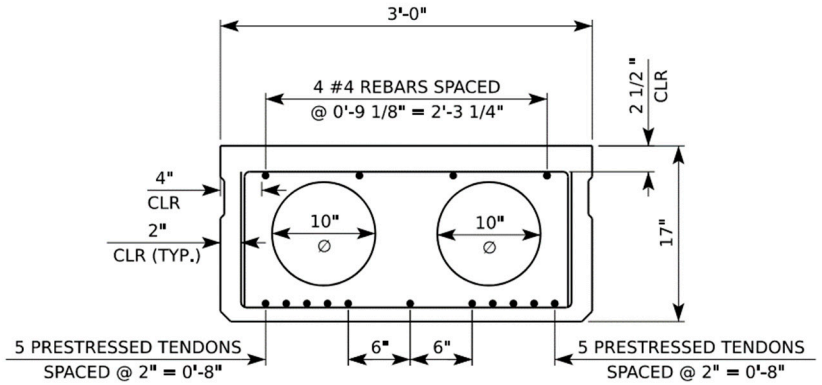

Figure 2. Prestressed concrete box beam typical section.

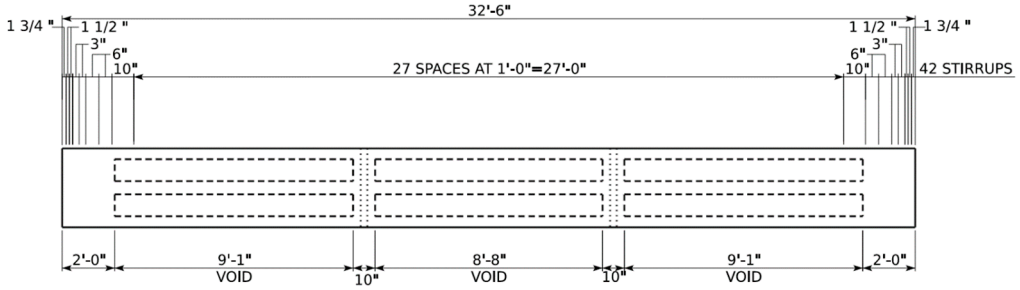

Figure 3. Prestressed concrete box beam plan view.

4.2. Data Collection and Acquisition

The prestressed concrete box beam underwent a comprehensive analysis on all sides. Each scan line and direction played a crucial role in extracting profile information of the structure. Different scanning directions were used based on the specific face being analyzed and the required information to be extracted below the surface. The top face was scanned both across and along the beam. A total of 97 transverse profile lines spaced 4.0 in. apart and 3 longitudinal lines spaced 11.0 in. apart were used. The transverse profiles mainly gathered information about the top longitudinal reinforcement, while the longitudinal profiles focused on the stirrup's information. The bottom face was only scanned across, using the same survey grid as the top face. Due to accessibility constraints, not all 97 profile lines were analyzed on the bottom face. The bottom profiles provided crucial information regarding prestressed tendons. The side faces of the beam were inspected using a single centrally positioned profile line. The longitudinal profile lines for the side faces were divided into three groups on each face due to the steel ducts used to connect the box beams. Figure 4 shows the layout of the survey grid used for data collection on the top face of the beam, with transverse profile lines numbered sequentially from 1 to 97, moving from left to right, and longitudinal profiles lines numbered from 1 to 3, from top to bottom. Table 1 displays the parameters used to analyze the concrete box beam.

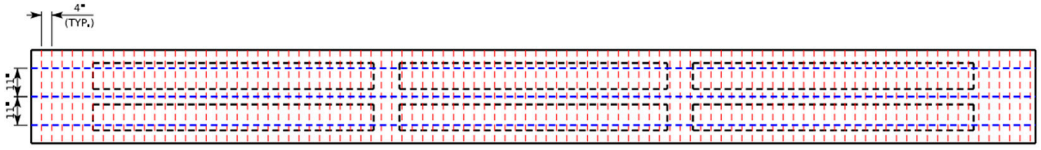

(**a**)

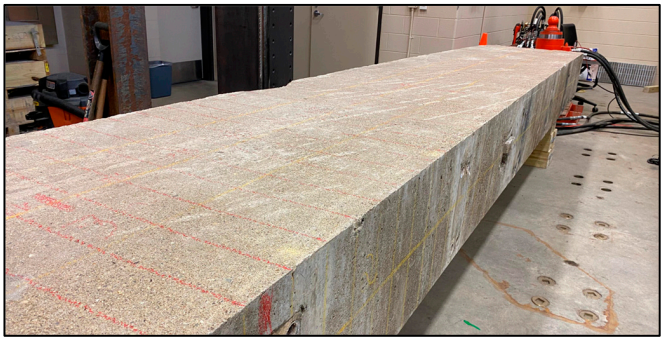

(**b**)

Figure 4. Prestressed concrete box beam survey grid; (**a**) top face transverse (red) and longitudinal (blue) profile lines; (**b**) prestressed concrete box beam top face transverse profile lines (red).

Table 1. Parameters of the GPR device.

Scan Parameters	Value
Samples per scan	2048
Scans per second	47
Scan per in.	20

5. Auto Rebar Picking

The shape of the hyperbola is a critical factor in GPR data processing, influenced by two parameters: (1) scan spacing, where shorter scan spacings (in/scan) result in wider parabolas, and (2) wave velocity, with lower dielectric constants (higher electromagnetic wave velocity) producing wider parabolas and vice versa. Additionally, larger targets generate brighter reflections; however, the change in the hyperbola shape for different target sizes is nearly negligible for any diameter under 2 in. due to target sizes being a

fraction of the electromagnetic wavelength. The theoretical equations of the hyperbola are derived based on the following assumptions [35]: (1) the signal reflected from a rebar is phase reversal indicating that the positive peaks of the reflected waves correspond to the negative peaks of the transmitted wave; (2) the reflected wave at the surface of the rebar is the shortest two-way travel path.

The length of traveling path of the signal reflected from a rebar can be obtained in the following equations, as shown in Figure 5:

$$L_1 = \sqrt{(z)^2 + \left(X - \frac{S}{2}\right)^2} \tag{1}$$

$$L_2 = \sqrt{(z)^2 + \left(X + \frac{S}{2}\right)^2} \tag{2}$$

where $X = x_p - x$ is the distance between the rebar and the center line of the transmitter and receiver in the horizontal direction; z represents the rebar depth; S is T-R offset of the antenna; x_p is the co-ordinate of the rebar in the horizontal direction; x is the co-ordinate of the antenna in the horizontal direction.

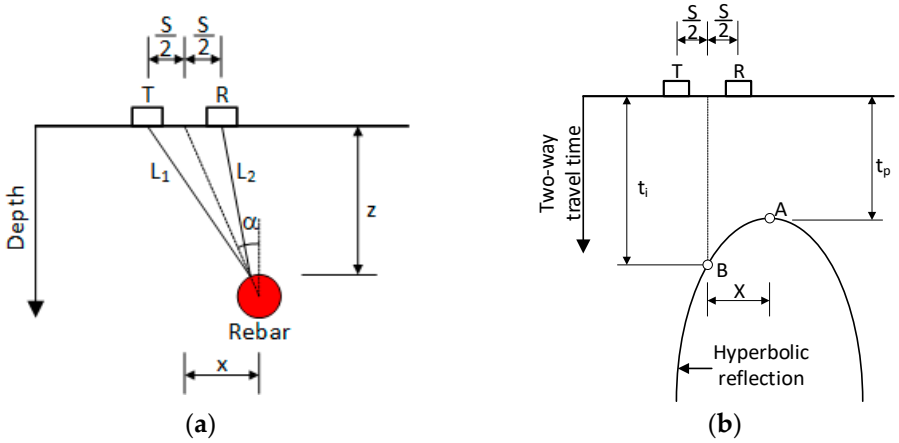

Figure 5. (**a**) EM wave travel path and (**b**) hyperbolic reflection from a rebar [35].

The relationship between two-wave travel time and path at the peak of the hyperbola is expressed as (Figure 5b):

$$t_p - t_0 = \frac{\sqrt{4z^2 + S^2}}{V_s} \tag{3}$$

where t_0 represents the time zero, indicating when the signal begins emitting into the medium, and t_p represents the time corresponding to the vertical co-ordinate of the peak of the hyperbola. The relationship between two-wave travel time and path can be obtained by employing Equation (3) as follows:

$$t_i - t_0 = \frac{L_1 + L_2}{V_s} \tag{4}$$

The traveling time of the signal is obtained by introducing Equations (1)–(3) into Equation (4) as in the following equation:

$$t_i = (t_p - t_0)\frac{\sqrt{(z)^2 + \left(X - \frac{S}{2}\right)^2} + \sqrt{(z)^2 + \left(X + \frac{S}{2}\right)^2}}{\sqrt{4z^2 + S^2}} + t_0 \tag{5}$$

Equation (5) represents the theoretical hyperbolic curve produced by a rebar embedded in reinforced concrete (RC) structures. However, the variations in hyperbolic curves corresponding to different rebar sizes are negligible.

The algorithm developed for this study processes GPR data to identify hyperbolic shapes in the radargram and extracts amplitude data for each hyperbolic peak. By comparing the amplitudes of these hyperbolic shapes with theoretical hyperbolas derived from Equation (5) and calculating the sum of squared differences (R^2), the program can determine whether the hyperbolic shapes represent rebar. Users can adjust the acceptable sum of squared differences to enhance the accuracy of rebar detection by setting a predefined threshold (Q). This study limited the difference between positive amplitude hyperbolic shapes from the GPR data and theoretical curves to 80%. Once the rebar is located by the algorithm, the rebar depth and location can be determined. The algorithm's flowchart is illustrated in Figure 6.

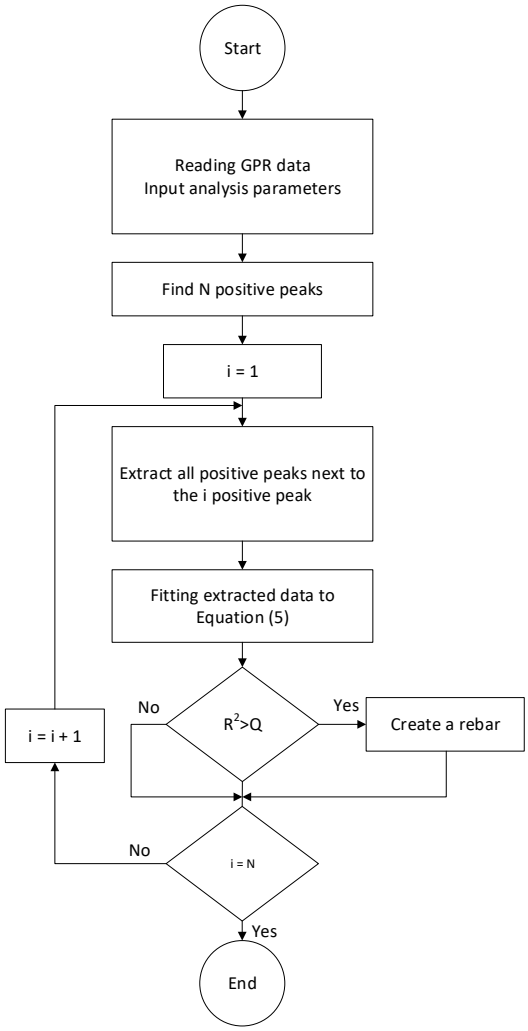

Figure 6. Flow chart.

6. Time Zero and Wave Velocity

To calculate the time zero in this study, the GPR device was placed on top of two foam objects and several profile samples were collected in the air. The scan data were then analyzed, and a time zero of approximately 13 ns was calculated using the equations provided by Zatar et al. [35].

The methods proposed by Wiwatrojanagul et al. [37] and Xing et al. [38,39] allow for the determination of electromagnetic wave velocity but require prior knowledge of the rebar size. Consequently, these methods are unsuitable for identifying unknown rebar sizes in concrete structures. To address this limitation, electromagnetic waves reflected from the bottom of the beam can be used to determine wave velocity using Equation (3). When the signal is weak, placing a metal plate on the beam's bottom face can magnify the

reflection [35]. However, due to the height of the concrete box beam used in this study, the electromagnetic waves do not reach the bottom face of the concrete structure. To address this limitation, the researchers estimated the electromagnetic wave velocity of the concrete box beam by correlating the two-way travel distance and time from the beam's top surface to the steel duct located inside of the structure. This duct is designed to connect the bridge's box beams with post-tensioned rods and is exposed at the side faces; therefore, the depth z of the duct can be accurately measured and the electromagnetic wave velocity is estimated using Equation (3).

7. Results and Discussion

The radargrams in Figure 7 represent typical profile images of the top and bottom faces of the prestressed concrete beam used in this study. Figure 7a reveals four longitudinal rebars at the top of the beam, represented by the dark red parabolas, and two air voids, represented by the dark red–blue parabolas below the top rebar row. Figure 7b shows a typical longitudinal profile image of the top face of the beam, revealing the total number and location of each stirrup. Figure 7c represents a typical bottom profile image, where the prestressed tendons are located.

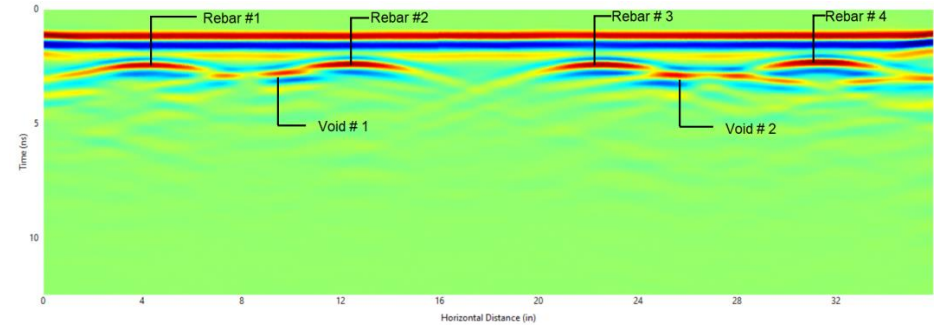

(**a**)

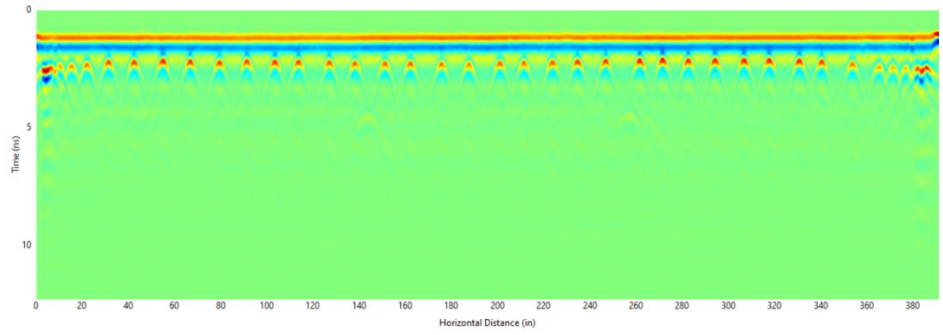

(**b**)

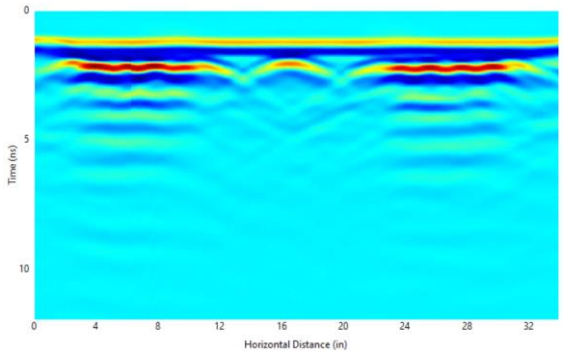

(**c**)

Figure 7. Typical profile images of the prestressed concrete beam: (**a**) top face transverse profile no. 15, (**b**) top face longitudinal profile no. 2, and (**c**) bottom face transverse profile no. 20.

The speed of the electromagnetic wave, a crucial component of the proposed methodology, was calculated to be 5.31 in. per nanosecond. This calculation was made by correlating Equations (2) and (3) with the vertical position of the steel duct inside the concrete box beam, which is located 7.375 inches below the top surface of the structure. The electromagnetic wave velocity is a crucial parameter in the GPR data analysis, since it enables the calculation of rebar depth, spacing, and concrete cover. The rebar data, which were initially calculated manually by analyzing the radargram for each GPR profile image, are now automatically determined using the algorithm developed for this paper. This new approach not only saves time but also ensures accuracy, making the process more reliable. The comparison of rebar location and depth between manual and automatic rebar detection using the methodology explained in this paper shows excellent agreement, as illustrated in Figures 8 and 9 for the main rebars and Figure 10 for the stirrups.

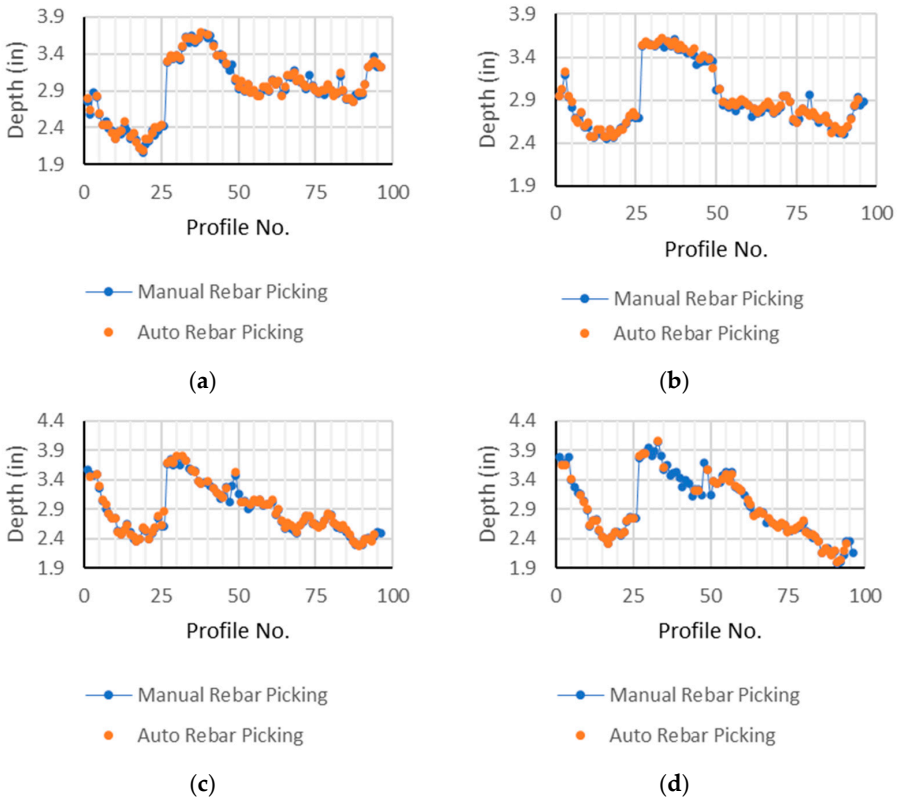

Figure 8. Rebar depth comparisons between manual and auto rebar picking for top rebars: (**a**) Rebar #1; (**b**) Rebar #2; (**c**) Rebar #3; and (**d**) Rebar #4.

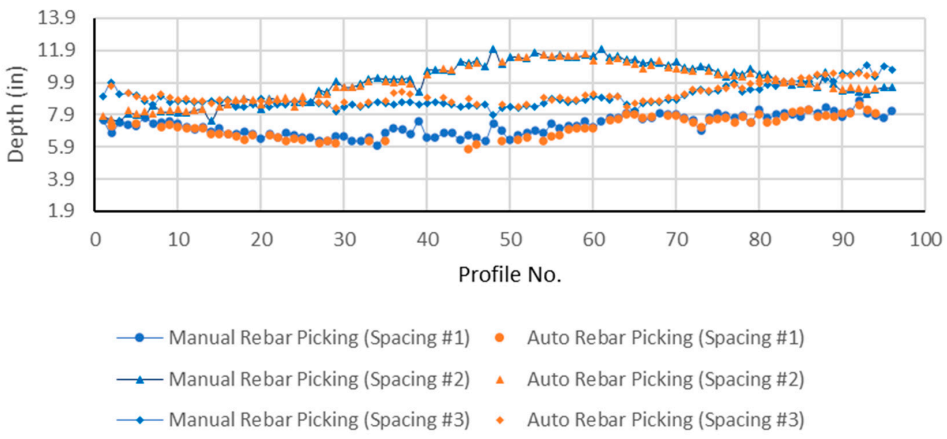

Figure 9. Rebar spacing comparisons between manual and auto rebar picking for top rebars.

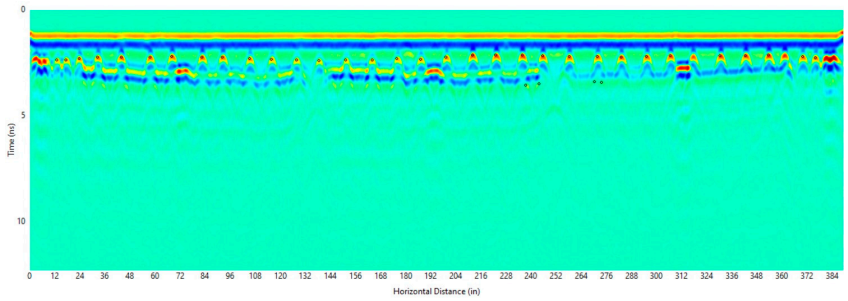

Figure 10. Auto rebar picking for stirrups (longitudinal profile no. 3).

Figures 8d and 9 show that the algorithm failed to detect the rebar near profile number 40. This was primarily due to significant signal interference from air voids and stirrups in that area, which prevented the algorithm from identifying the positive amplitude curves using the 80% threshold (Q) set for this analysis. While reducing the acceptable sum of squared differences between the theoretical and actual hyperbolic curves could help improve rebar detection, it likely leads to many false positives, complicating the data analysis further. Therefore, it is necessary to manually analyze locations where the automatic algorithm is unable to detect rebar because of inconsistencies in the GPR reconstructed image.

Figure 10 illustrates the locations where the algorithm identified the stirrups, demonstrating high accuracy, with only four false positives. This performance is largely attributed to the minimal electromagnetic signal interference in the longitudinal profiles, where the air voids are situated far from the stirrups, and there is a clear path between the stirrups and the concrete surface. Similar to the manual data collection, the algorithm failed to detect the stirrups at the ends of the beam due to the tight spacing regime and high EM signal overlap. While the longitudinal profiles proved particularly effective for the automatic rebar detection algorithm, it is important to note that transverse profiles also yielded accurate results. Both scan orientations contribute valuable insights, with the longitudinal profiles offering a slight advantage in terms of clarity due to the reduced electromagnetic signal interference.

Although the algorithm failed to calculate rebar depth and spacing in some locations, this novel methodology offers a significant advantage over existing research by eliminating the need for template selection and extensive algorithm development based on an infinite dataset of hyperbolic shapes, as proposed by previous studies [40,41]. Additionally, hyperbolic shapes are not only associated with rebar in RC; thus, relying on templates can lead to false positives due to various hyperbolic shapes in the concrete. The algorithm developed in this study utilizes typical amplitude patterns of electromagnetic wave reflections from rebar, effectively reducing the likelihood of assigning random hyperbolic shapes in the RC as rebar.

After validating the accuracy of manual data through automatic rebar detection, the research focused on analyzing the impact of different transverse and longitudinal GPR scan line offsets on the results. The core objective was to determine whether reducing the number of scan lines during data collection still provides comprehensive insight into the inner characteristics of reinforced concrete structures, such as rebar configuration and potential deficiencies. By minimizing data collection points while maintaining the reliability of profile data, this approach will enhance both the efficiency and accuracy of bridge inspections using GPR technology.

Figure 11 illustrates the comparison of rebar depth for transverse profile spacings ranging from 4 in. to 24 in., while Figure 12 shows the comparison for rebar spacing. The results are summarized in Tables 2 and 3. Discrepancies between the calculated values and the information provided in Figure 2 were found to be associated with construction flaws, as the GPR device was specifically calibrated for the concrete box beam discussed in this paper and due to the consistency among different profile lines.

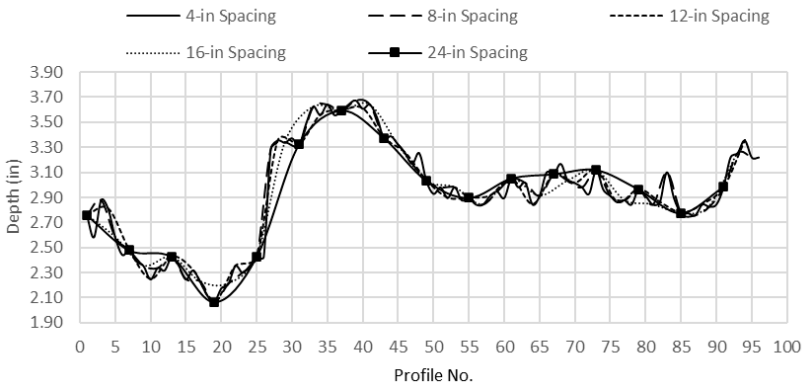

(**a**)

(**b**)

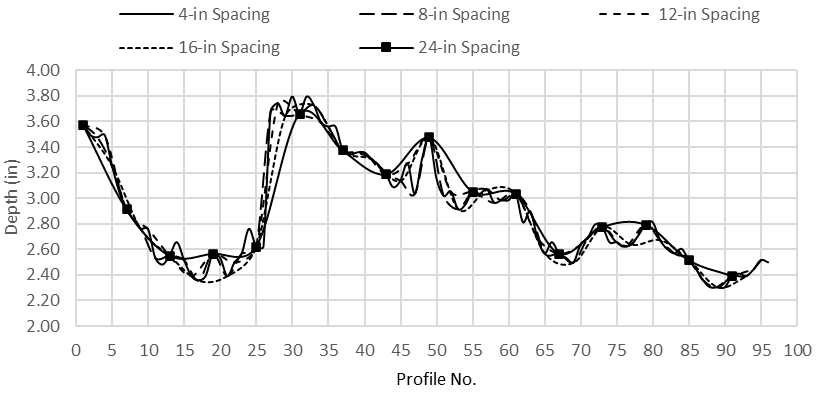

(**c**)

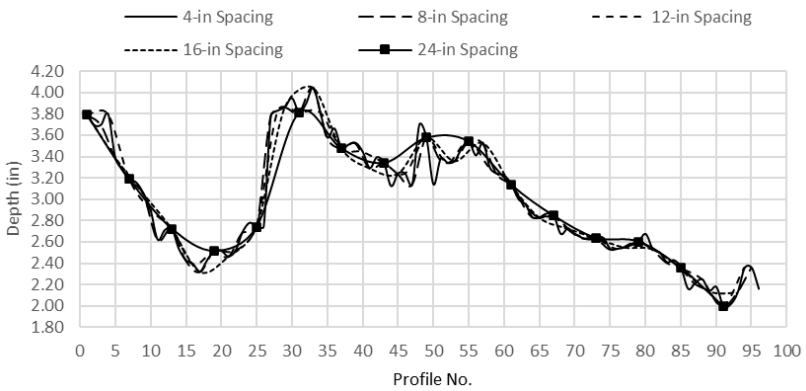

(**d**)

Figure 11. Top reinforcement row depth: (**a**) Rebar #1; (**b**) Rebar #2; (**c**) Rebar #3; and (**d**) Rebar #4.

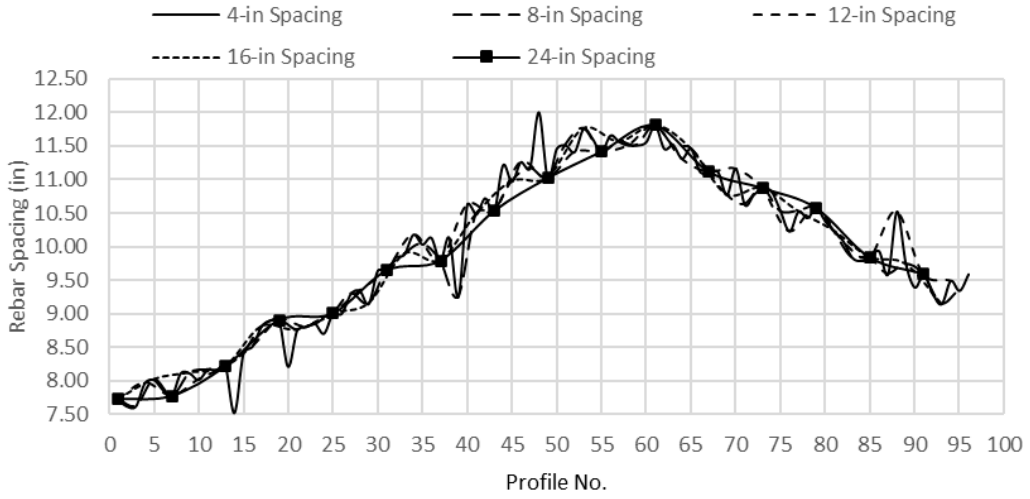

(**a**)

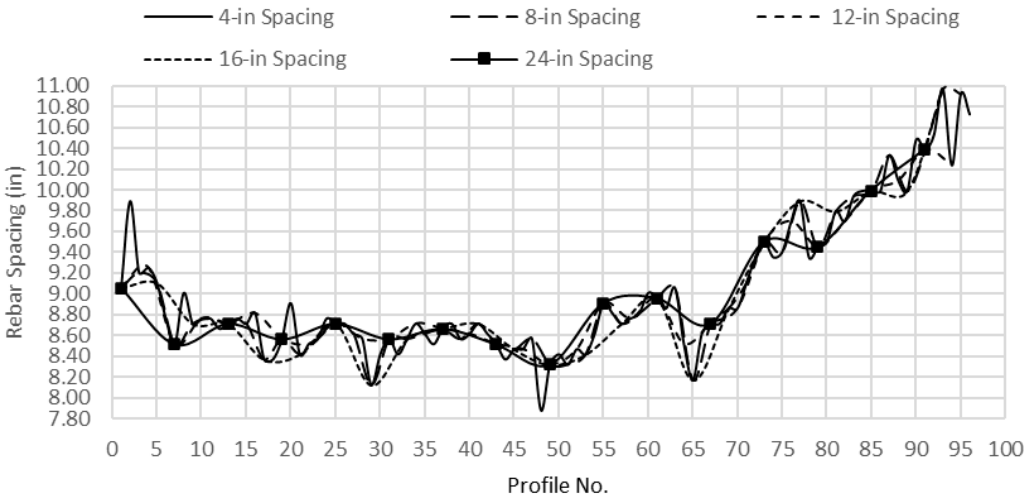

(**b**)

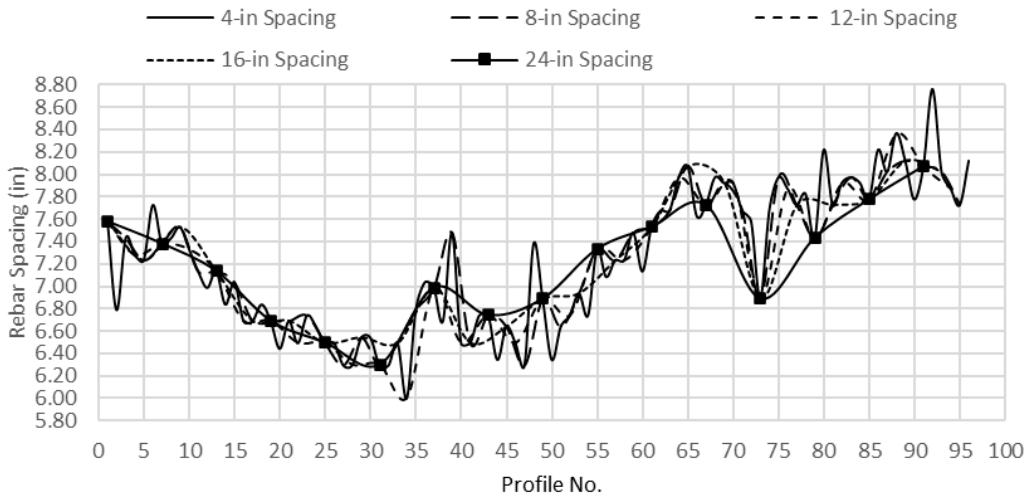

(**c**)

Figure 12. Top reinforcement row spacing: (**a**) Space #1, (**b**) Space #2; and (**c**) Space #3.

Table 2. (**a**) Top rebars' depth for different GPR profile offsets; (**b**) top rebars' horizontal spacing for different GPR profile offsets.

(a)			
Profile Spacing	**Depth [1] (in)**	**Calculated Depth [2] (in)**	**Difference [3]**
4-in	2.50	2.92	17%
8-in	2.50	2.93	17%
12-in	2.50	2.94	18%
16-in	2.50	2.93	17%
24-in	2.50	2.94	18%

(b)						
Profile Spacing	**Horizontal Clearance [1] (in)**	**Calculated Horizontal Clearance [2] (in)**	**Difference [3]**	**Spacing [1] (in)**	**Calc. Spacing [2] (in)**	**Difference [3]**
4-in	4.00	4.90	22%	9.12	8.74	−4%
8-in	4.00	4.90	23%	9.12	8.73	−4%
12-in	4.00	4.92	23%	9.12	8.72	−4%
16-in	4.00	4.91	23%	9.12	8.72	−4%
24-in	4.00	4.96	24%	9.12	8.69	−5%

[1] Value extracted from existing beam drawing. [2] Average values calculated from the analysis of the GPR profiles. [3] Rounded percent difference between the expected values from the drawing and the actual measurements.

Table 3. Top longitudinal rebar minimum and maximum calculated depth and spacing values.

	Calculated Depth (in)	**Calculated Horizontal Concrete Cover (in)**	**Calculated Spacing (in)**
Minimum	2.93	4.90	8.69
Maximum	2.94	4.96	8.74
Variance	0.01	0.06	0.05

Figures 11 and 12 demonstrate that all transverse profile offsets show nearly identical rebar spacing and depth patterns for the structure. The average calculated values in Table 2 are nearly the same for all profile line offsets, with minimal variation. Table 3 shows the minimum and maximum calculated values for the rebar depth, horizontal concrete cover, and spacing among the transverse profile offsets ranging from 4 in. to 24 in. The consistency between the results suggests that different transverse profile line offsets have a minimal effect on the accuracy of the depth and spacing measurements of the top longitudinal reinforcement.

Similar to the top transverse profile offsets, the effects of different spacing on GPR data collection for the longitudinal profile lines were also analyzed. In comparing one profile line versus three profile lines in the top longitudinal scans, no significant difference was found. The original plans indicated that the concrete box beam under study contains 41 stirrups, while the analysis of the GPR data identified 34 stirrups. The variation in the number of stirrups can be attributed to closely spaced shear reinforcement at both ends of the beam, making it difficult to accurately read the rebars due to the high electromagnetic conductivity in the area. Consequently, the precise number of stirrups could not be determined. However, the longitudinal profile image indicates a greater concentration of shear reinforcement at the end of the beam, which aligns with the typical characteristics of prestressed concrete box beams.

Results for one and three longitudinal profile lines along the top face of the beam are summarized in Table 4. Maximum and minimum values calculated for the depth and spacing of the stirrups are shown in Table 5. While there is no significant difference between using one or three profile lines to ascertain shear reinforcement information, using only one longitudinal profile line could lead to the loss of valuable internal information. For example, with a single profile line running along the center of the beam, the internal voids of the

concrete would not be fully visible, potentially leading engineers to mistakenly believe that no voids exist. To ensure a more comprehensive assessment, using three longitudinal scans per beam is highly advisable, though the precise number of scans should be determined based on a thorough evaluation of the specific bridge conditions. This approach ensures a more complete understanding of the beam's internal features and improves the overall reliability of the detection process.

Table 4. Shear reinforcement spacing and depths for different numbers of GPR profile lines.

Longitudinal Profile Layout	Depth [1] (in)	Calculated Depth [2] (in)	Depth Diff. [3]	Spacing [1] (in)	Calculated Spacing [2] (in)	Space Diff. [3]
1 Profile line (Center)	2.0	2.35	18%	12.0	11.83	1%
2 Profile Lines	2.0	2.38	19%	12.0	11.89	1%
3 Profile Lines	2.0	2.37	19%	12.0	11.87	1%

[1] Value extracted from existing beam drawing. [2] Average values calculated from the analysis of the GPR profiles. [3] Rounded percent difference between the expected values from the drawing and the actual measurements.

Table 5. Shear reinforcement minimum and maximum calculated rebar depth and spacing values.

	Depth (in)	Spacing (in)
Minimum	2.35	11.83
Maximum	2.37	11.89
Variance	0.02	0.06

Finally, the effects of profile line offsets on the bottom face of the concrete box beam were evaluated. Similar to the top transverse profile lines, different bottom profile line offsets consistently resulted in similar results for rebar spacing and depth, regardless of the offset between the profile lines. Table 6 summarizes the results of the average calculated depth and spacing values for the prestressed tendons.

Table 6. (**a**) Two sets of prestressed tendons' depth and spacing for different GPR profile offsets; (**b**) center prestressed tendon depth and spacing values for different GPR profile offsets.

(a)						
Two Sets of 5 Prestressed Tendons						
Profile Spacing	**Depth [1] (in)**	**Calculated Depth [2] (in)**	**Difference [3]**	**Spacing [1] (in)**	**Calculated Spacing [2] (in)**	**Difference [3]**
4-in	2.0	1.82	−9%	2.0	1.88	−6%
8-in	2.0	1.86	−7%	2.0	1.87	−6%
12-in	2.0	1.86	−7%	2.0	1.88	−6%
16-in	2.0	1.83	−9%	2.0	1.88	−6%
24-in	2.0	1.83	−8%	2.0	1.87	−7%
(**b**)						
Center Prestressed Tendon						
Profile Spacing	**Depth [1] (in)**	**Calculated Depth [2] (in)**	**Difference [3]**	**Spacing [1] (in)**	**Calculated Spacing [2] (in)**	**Difference [3]**
4-in	2.0	1.54	−23%	6.0	5.50	−8%
8-in	2.0	1.59	−20%	6.0	5.52	−8%
12-in	2.0	1.59	−21%	6.0	5.52	−8%
16-in	2.0	1.54	−23%	6.0	5.50	−8%
24-in	2.0	1.57	−21%	6.0	5.54	−8%

[1] Value extracted from existing beam drawing. [2] Average values calculated from the analysis of the GPR profiles. [3] Rounded percent difference between the expected values from the drawing and the actual measurements.

The calculated values were consistent with the beam's drawing, with depth and spacing variations of less than 10% for the two sets of prestressed tendons on each side of the box beam. However, the center prestressed tendon showed significant discrepancies, with differences of up to 23% compared to the drawing values. These variations in the center prestressed tendon are significant. Given the consistency of the calculated rebar depths and the GPR device calibration specifically for this concrete box beam, the difference between the calculated values and the depths shown in Figure 2 is attributed to construction flaws. A summary of the maximum and minimum values calculated for different GPR profile offsets is provided in Table 7.

Table 7. Bottom prestressed tendons' minimum and maximum calculated depth and spacing values.

Structure	Two Sets of Prestressed Tendons		Center Prestressed Tendon	
	Depth (in)	Spacing (in)	Depth (in)	Spacing (in)
Minimum	1.82	1.87	1.54	5.50
Maximum	1.86	1.88	1.59	5.54
Variance	0.04	0.01	0.05	0.04

8. Limitations

The authors of this study recognize that, while analyzing the three prestressed concrete box beams provides accurate and reliable information about the condition of reinforced concrete structures, several points need to be addressed to fully comply with the optimal protocol for using GPR technology in bridge inspections.

The researchers noted the first limitation, which was the calculation of the wave velocity of the electromagnetic waves. This parameter is crucial for accurately calculating rebar depths, spacing, and sizes. For this study, the wave velocity was calculated using the travel–time and travel–distance relationship to a known object, which was the steel duct used for the post-tensioned rods. This may pose a limitation in real-world applications, as accurately calculating the wave velocity without internal information about the reinforced concrete structure is challenging. Although bridge inspectors can see the steel duct, calculating the precise depth is difficult.

Additionally, this study did not consider the effect of environmental factors, such as temperature and humidity, on the accuracy of GPR scans. This could be a limitation in real-world bridge inspection scenarios. Another aspect that requires further evaluation is accessibility to the bottom face of the structure and how to assist bridge inspectors in transversely scanning the bottom face with ease.

9. Conclusions

This study aimed to determine the best transverse and longitudinal GPR profile line spacing offset. The method involved calculating the depth and spacing of rebars on each face of the beam by measuring the travel time of electromagnetic waves. This was achieved by conducting a series of GPR scans at different offsets and analyzing the hyperbolas recorded by the GPR. A custom computer code was created to automatically determine the depth and location of the rebar based on these hyperbolas.

This study concluded that GPR profile line offsets do not significantly affect the results. Transverse profile line spacings ranging from 4 in. to 24 in. produced nearly identical results. Similarly, the number of longitudinal profile lines did not affect the stirrup depths and spacing results. However, it was found that the voids inside the concrete could not be determined with a single GPR profile line. Therefore, to ensure a thorough and accurate assessment of the prestressed concrete box beams, bridge inspectors must conduct multiple longitudinal profile scans, with a minimum of three scans being essential for a complete understanding of the internal features.

The consistency in the study results provides a strong foundation for the study's reliability. The findings can enhance the efficiency and accuracy of bridge evaluations by

helping bridge inspectors determine internal characteristics of prestressed concrete box beams, including rebar spacing, depth, sizes, and internal deficiencies. The study's findings offer valuable advancements and empower state departments of transportation with the knowledge to assess in-service concrete bridge box beams accurately, enabling them to make informed decisions about their bridge maintenance and repair strategies.

Author Contributions: Conceptualization, W.Z., F.M.R. and H.N.; methodology, F.M.R. and H.N.; software, H.N.; validation W.Z., F.M.R. and H.N.; formal analysis, F.M.R.; investigation, F.M.R.; resources, W.Z.; data curation, F.M.R.; writing—original draft preparation, F.M.R. and H.N.; writing—review and editing, W.Z.; visualization, W.Z.; supervision, W.Z.; project administration, W.Z.; funding acquisition, W.Z. All authors have read and agreed to the published version of the manuscript.

Funding: This research was funded by West Virginia Department of Transportation grant number [RP328].

Institutional Review Board Statement: Not applicable.

Informed Consent Statement: Not applicable.

Data Availability Statement: The data presented in this study are available on request from the corresponding author (due to restrictions from the funding agency).

Acknowledgments: The authors would like to express their sincere gratitude for the financial support provided by the West Virginia Department of Transportation, Division of Highways (WVDOH), for funding this research project. This support was instrumental in completing the study and is greatly appreciated. It is essential to clarify that the findings, conclusions, and recommendations presented in this study reflect the authors' perspectives and do not necessarily represent the views of WVDOH.

Conflicts of Interest: The authors declare no conflicts of interest.

References

1. Kaiser, H.; Karbhari, V.M.; Sikorsky, C. Non-destructive testing techniques for FRP rehabilitated concrete. II: An assessment. *Int. J. Mater. Prod. Technol.* **2004**, *21*, 385–401. [CrossRef]
2. Büyüköztürk, O. Imaging of concrete structures. *NDT E Int.* **1998**, *31*, 233–243. [CrossRef]
3. Popovics, J.S.; Roesler, J.R.; Bittner, J.; Amirkhanian, A.N.; Brand, A.S.; Gupta, P.; Flowers, K. *Ultrasonic Imaging for Concrete Infrastructure Condition Assessment and Quality Assurance*; Illinois Center for Transportation Series No. 17-011, Research Report No. FHWA-ICT-17-007; Illinois Center for Transportation: Rantoul, IL, USA, 2017.
4. Zhu, J.; Wang, Y.; Qing, X. A real-time electromechanical impedance-based active monitoring for composite patch bonded repair structure. *Compos. Struct.* **2019**, *212*, 513–523. [CrossRef]
5. Naoum, M.C.; Sapidis, G.M.; Papadopoulos, N.A.; Voutetaki, M.E. An Electromechanical Impedance-Based Application of Realtime Monitoring for the Load-Induced Flexural Stress and Damage in Fiber-Reinforced Concrete. *Fibers* **2023**, *11*, 34. [CrossRef]
6. Rao, R.K.; Sasmal, S. Electromechanical impedance-based embeddable smart composite for condition-state monitoring. *Sens. Actuators Phys.* **2022**, *346*, 113856. [CrossRef]
7. Fan, L.; Bao, Y. Review of fiber optic sensors for corrosion monitoring in reinforced concrete. *Cem. Concr. Compos.* **2021**, *120*, 104029. [CrossRef]
8. Berrocal, C.G.; Fernandez, I.; Rempling, R. Crack monitoring in reinforced concrete beams by distributed optical fiber sensors. *Struct. Infrastruct. Eng.* **2021**, *17*, 124–139. [CrossRef]
9. Khan, A.Z.; Stanbridge, A.B.; Ewins, D.J. Detecting damage in vibrating structures with a scanning LDV. *Opt. Lasers Eng.* **1999**, *32*, 583–592. [CrossRef]
10. Wang, Z.; Wang, K.; Han, Q.; Ni, J.; Wu, Z. Crack imaging of underwater concrete components using interfacial waves and transducer array. *Mech. Syst. Signal Process.* **2025**, *224*, 111998. [CrossRef]
11. ACI Committee 228. *Report on Nondestructive Test Methods for Evaluation of Concrete in Structures*; Report ACI 228.2R-13; American Concrete Institute: Indianapolis, IN, USA, 2013.
12. Alani, A.M.; Aboutalebi, M.; Kilic, G. Applications of ground penetrating radar (GPR) in bridge deck monitoring and assessment. *J. Appl. Geophys.* **2013**, *97*, 45–54. [CrossRef]
13. He, X.Q.; Zhu, Z.Q.; Liu, Q.Y.; Lu, G.Y. Review of GPR rebar detection. In Proceedings of the PIERS, Moscow, Russia, 18–21 August 2009; pp. 804–813.
14. Bala, D.C.; Garg, R.D.; Jain, S.S. Rebar detection using GPR: An emerging non-destructive QC approach. *Int. J. Eng. Res. Appl.* **2011**, *1*, 2111–2117.
15. Hasan, M.I.; Yazdani, N. An experimental study for quantitative estimation of rebar corrosion in concrete using ground penetrating radar. *J. Eng.* **2016**, *2016*, 8536850. [CrossRef]

16. Hugenschmidt, J. Concrete bridge inspection with a mobile GPR system. *Constr. Build. Build. Mater.* **2002**, *16*, 147–154. [CrossRef]
17. Hasan, M.I.; Yazdani, N. Ground penetrating radar utilization in exploring inadequate concrete covers in a new bridge deck. *Case Stud. Constr. Mater.* **2014**, *1*, 104–114. [CrossRef]
18. Laurens, S.; Balayssac, J.P.; Rhazi, J.; Klysz, G.; Arliguie, G. Non-destructive evaluation of concrete moisture by GPR: Experimental study and direct modeling. *Mater. Struct.* **2005**, *38*, 827–832. [CrossRef]
19. Gucunski, N.; Rascoe, C.; Parrillo, R.; Roberts, R.L. Complementary Condition Assessment of Bridge Decks by High-Frequency Ground-Penetrating Radar and Impact Echo. No. 09-1282. 2009. Available online: https://trid.trb.org/View/881090 (accessed on 19 May 2009).
20. Benedetto, A.; Manacorda, G.; Simi, A.; Tosti, F. Novel perspectives in bridges inspection using GPR. *Nondestruct. Test. Eval.* **2012**, *27*, 239–251. [CrossRef]
21. Eisenmann, D.; Margetan, F.; Chiou, C.P.T.; Roberts, R.; Wendt, S. Ground penetrating radar applied to rebar corrosion inspection. *AIP Conf. Proc.* **2013**, *1511*, 1341–1348.
22. Zaki, A.; Johari, M.; Azmi, M.; Hussin, W.; Aminuddin, W.M.; Jusman, Y. Experimental Assessment of Rebar Corrosion in Concrete Slab Using Ground Penetrating Radar (GPR). *Int. J. Corros.* **2018**, *2018*, 5389829. [CrossRef]
23. Eisenmann, D.; Margetan, F.J.; Koester, L.; Clayton, D. Inspection of a large concrete block containing embedded defects using ground penetrating radar. *AIP Conf. Proc.* **2016**, *1706*, 020014.
24. Garg, S.; Misra, S. Efficiency of NDT techniques to detect voids in grouted post-tensioned concrete ducts. *Nondestruct. Test. Eval.* **2020**, *36*, 366–387. [CrossRef]
25. Yehia, S.; Qaddoumi, N.; Farrag, S.; Hamzeh, L. Investigation of concrete mix variations and environmental conditions on defect detection ability using GPR. *NDT E Int.* **2014**, *65*, 35–46. [CrossRef]
26. Tarussov, A.; Vandry, M.; De La Haza, A. Condition assessment of concrete structures using a new analysis method: Groundpenetrating radar computer-assisted visual interpretation. *Constr. Build. Mater.* **2013**, *38*, 1246–1254. [CrossRef]
27. Zatar, W.; Nghiem, H. Detectability of Embedded Defects in FRP Strengthened Concrete Deck Slabs. In *Risk-Based Strategies for Bridge Maintenance*; CRC Press: Boca Raton, FL, USA, 2023; pp. 221–234.
28. Hugenschmidt, J.; Kalogeropoulos, A.; Soldovieri, F.; Prisco, G. Processing strategies for high-resolution GPR concrete inspections. *NDT E Int.* **2010**, *43*, 334–342. [CrossRef]
29. Zatar, W.; Nguyen, T.; Nguyen, H. Environmental effects on condition assessments of concrete structures with ground penetrating radar. *J. Appl. Geophys.* **2022**, *203*, 104713. [CrossRef]
30. Zatar, W.A.; Nguyen, T.; Nguyen, H.D. Predicting GPR signals from concrete structures using artificial intelligence-based method. *Adv. Civ. Eng.* **2021**, *2021*, 6610805. [CrossRef]
31. Zhang, Y.C.; Du, Y.L.; Yi, T.H.; Zhang, S.H. Automatic Rebar Picking for Corrosion Assessment of RC Bridge Decks with Ground-Penetrating Radar Data. *J. Perform. Constr. Facil.* **2024**, *38*, 04023069. [CrossRef]
32. Faris, N.; Zayed, T.; Fares, A.; Abdelkhalek, S.; Abdelkader, E.M. Automated rebar recognition and corrosion assessment of concrete bridge decks using ground penetrating radar. *Autom. Constr.* **2024**, *166*, 105631. [CrossRef]
33. Shu, J.; Zhang, X.; Li, W.; Zeng, Z.; Zhang, H.; Duan, Y. Point cloud and machine learning-based automated recognition and measurement of corrugated pipes and rebars for large precast concrete beams. *Autom. Constr.* **2024**, *165*, 105493. [CrossRef]
34. Zatar, W.A.; Nguyen, H.D.; Nghiem, H.M. Ultrasonic pitch and catch technique for non-destructive testing of reinforced concrete slabs. *J. Infrastruct. Preserv. Resil.* **2020**, *1*, 12. [CrossRef]
35. Zatar, W.; Nghiem, H.; Nguyen, H. Detecting Reinforced Concrete Rebars Using Ground Penetrating Radars. *Appl. Sci.* **2024**, *14*, 5808. [CrossRef]
36. GSSI. Concrete Handbook, GPR Inspection of Concrete. Available online: https://www.geophysical.com/wp-content/uploads/2017/10/GSSI-Concrete-Handbook.pdf (accessed on 12 September 2024).
37. Wiwatrojanagul, P.; Sahamitmongkol, R.; Tangtermsirikul, S.; Khamsemanan, N. A new method to determine locations of rebars and estimate cover thickness of RC structures using GPR data. *Constr. Build. Mater.* **2017**, *140*, 257–273. [CrossRef]
38. Xiang, Z.; Ou, G.; Rashidi, A. Integrated approach to simultaneously determine 3D location and size of rebar in GPR data. *J. Perform. Constr. Facil.* **2020**, *34*, 04020097. [CrossRef]
39. Xiang, Z.; Ou, G.; Rashidi, A. An Innovative Approach to Determine Rebar Depth and Size by Comparing GPR Data with a Theoretical Database. In *Construction Research Congress*; American Society of Civil Engineers: Reston, VA, USA, 2020; pp. 86–95.
40. Ma, X.; Liu, H.; Wang, M.L.; Birken, R. Automatic Detection of Steel Rebar in Bridge Decks from Ground Penetrating Radar Data. *J. Appl. Geophys.* **2018**, *158*, 93–102. [CrossRef]
41. Shaw, M.R.; Millard, S.G.; Molyneaux, T.C.K.; Taylor, M.J.; Bungey, J.H. Location of Steel Reinforcement in Concrete Using Ground Penetrating Radar and Neural Networks. *NDT E Int.* **2005**, *38*, 203–212. [CrossRef]

Disclaimer/Publisher's Note: The statements, opinions and data contained in all publications are solely those of the individual author(s) and contributor(s) and not of MDPI and/or the editor(s). MDPI and/or the editor(s) disclaim responsibility for any injury to people or property resulting from any ideas, methods, instructions or products referred to in the content.